





# Discovery of radio jets in the Phoenix galaxy cluster center

Takuya AKAHORI <sup>1,\*</sup>, Tetsu KITAYAMA,<sup>2</sup> Shutaro UEDA <sup>3,4</sup>, Takuma IZUMI,<sup>4</sup>  
Kianhong LEE <sup>5</sup>, Ryohei KAWABE,<sup>4,6,7</sup> Kotaro KOHNO <sup>5,8</sup>,  
Masamune OGURI,<sup>8,9,10</sup> and Motokazu TAKIZAWA<sup>11</sup>

<sup>1</sup>Mizusawa VLBI Observatory, National Astronomical Observatory of Japan, 2-21-1 Osawa, Mitaka, Tokyo 181-8588, Japan

<sup>2</sup>Department of Physics, Toho University, 2-2-1 Miyama, Funabashi, Chiba 274-8510, Japan

<sup>3</sup>Academia Sinica Institute of Astronomy and Astrophysics (ASIAA), No. 1, Section 4, Roosevelt Road, Taipei 10617, Taiwan

<sup>4</sup>National Astronomical Observatory Japan, 2-21-1 Osawa, Mitaka, Tokyo 181-8588, Japan

<sup>5</sup>Institute of Astronomy, The University of Tokyo, 2-21-1 Osawa, Mitaka, Tokyo 181-0015, Japan

<sup>6</sup>The Graduate University for Advanced Studies (SOKENDAI), 2-21-1 Osawa, Mitaka, Tokyo 181-8588, Japan

<sup>7</sup>Department of Astronomy, The University of Tokyo, 7-3-1 Hongo, Bunkyo, Tokyo 113-0033, Japan

<sup>8</sup>Research Center for the Early Universe, The University of Tokyo, 7-3-1 Hongo, Bunkyo-ku, Tokyo 113-0033, Japan

<sup>9</sup>Department of Physics, The University of Tokyo, 7-3-1 Hongo, Bunkyo-ku, Tokyo 113-0033, Japan

<sup>10</sup>Kavli Institute for the Physics and Mathematics of the Universe (Kavli IPMU, WPI), The University of Tokyo, Kashiwa, Chiba 277-8583, Japan

<sup>11</sup>Department of Physics, Yamagata University, 1-4-12 Kojirakawa-machi, Yamagata, Yamagata 990-8560, Japan

\*E-mail: [takuya.akahori@nao.ac.jp](mailto:takuya.akahori@nao.ac.jp)

Received 2019 March 29; Accepted 2020 April 12

## Abstract

We report the results of the Australia Telescope Compact Array (ATCA) 15 mm observation of the Phoenix galaxy cluster possessing an extreme star-burst brightest cluster galaxy (BCG) at the cluster center. We spatially resolved radio emission around the BCG, and found diffuse bipolar and bar-shape structures extending from the active galactic nucleus (AGN) of the BCG. They are likely radio jets/lobes, whose sizes are  $\sim 10$ – $20$  kpc and locations are aligned with X-ray cavities. If we assume that the radio jets/lobes expand with the sound velocity, their ages are estimated to be  $\sim 10$  Myr. We also found compact radio emissions near the center and suggest that they are more young bipolar jets  $\sim 1$  Myr in age. Moreover, we found extended radio emission surrounding the AGN and discussed the possibility that the component is a product of the cooling flow, by considering synchrotron radiation partially absorbed by molecular clumps, free-free emission from the warm ionized gas, and the spinning dust emission from the dusty circumgalactic medium.

**Key words:** galaxies: clusters: individual (Phoenix) — galaxies: individual (SPT-CL J2344–4243) — radio continuum: galaxies — X-rays: galaxies: clusters

## 1 Introduction

A galaxy cluster is permeated with the hot intra-cluster medium (ICM) emitting electron thermal bremsstrahlung and metal line-emission in X-ray. If only the loss of thermal energy by the X-ray radiation is realized, it leads to the quasi-hydrostatic evolution of the ICM under the gravitational potential (Masai & Kitayama 2004; Akahori & Masai 2006), and results in a catastrophic cooling-flow of a huge amount of cooled ICM at the cluster center (see Fabian 1994 for a review). X-ray observations, however, have found no such massive cooled gas at the centers of nearby clusters (e.g., Tamura et al. 2001; Makishima et al. 2001; Lewis et al. 2002; Peterson et al. 2003). Instead, many clusters possess the bottom of the ICM temperature, called the “cool-core” (e.g., Sanderson et al. 2009). The core radius, within which a radial profile of the ICM density has a flat slope, of a cool-core cluster tends to be one third of those of other relaxed clusters (Ota & Mitsuda 2002, 2004).

Cool-core clusters tend to possess cD galaxies or central brightest cluster galaxies (BCGs) (e.g., Akahori & Masai 2005), which often exhibit active galactic nucleus (AGN) jets. It has been considered that energy injection by the jets suppresses runaway cooling of the ICM and forms its cool-core profile, known as the AGN feedback scenario (e.g., Ruszkowski et al. 2004; Fabian 2012 for a review). Massive star-burst activities expected under the classical cooling-flow should also be suppressed in central galaxies because there is less inflow of cooled gas. In fact, BCGs are giant elliptical galaxies which are inactive star-forming systems in general, although minor star-forming activities can be seen in the local Universe; NGC 1275 in the Perseus cluster hosts blue, young star clusters (Holtzman 1992; Conselice et al. 2001) and star-forming regions (Canning et al. 2014).

The Phoenix galaxy cluster (SPT-CL J2344–4243) seems to be an exception from the picture established in the local Universe. The Phoenix cluster is a distant cluster located at the redshift of  $z = 0.596$ . It is a very massive cluster with a mass of  $2.5 \times 10^{15} M_{\odot}$  within the virial radius (McDonald et al. 2012). One of the spectacular features of this cluster is that the BCG possesses an unprecedented star-burst of  $800 M_{\odot} \text{ yr}^{-1}$  (McDonald et al. 2012, 2013). Moreover, it is suggested that the BCG possesses an ultra-heavy ( $1.8 \times 10^{10} M_{\odot}$ ) and fast-growing ( $60 M_{\odot} \text{ yr}^{-1}$ ) super-massive black hole (SMBH) (McDonald et al. 2013). Around the SMBH, huge cold molecular gas of  $2.1 \times 10^{10} M_{\odot}$  is expected according to the intensity of the carbon monoxide line, CO(3–2) (Russell et al. 2017). Based on the X-ray luminosity and its intrinsic absorption (Ueda et al. 2013), this AGN is classified as a type-2 quasar, which is quite rare in BCGs (only two samples known to-date). These

features imply that the massive cold-gas inflow expected in the classical cooling-flow scenario is realized in the Phoenix cluster (McDonald et al. 2012, 2013, 2014, 2015).

While the Phoenix cluster center exhibits some indirect evidence of classical cooling-flow, it is notable that the surrounding environment is rather similar to those in nearby cool-core clusters. For example, the global X-ray morphology is symmetric and round, so that it is unlikely that a major merger of clusters is taking place. Ueda et al. (2013) found that the global ICM temperature structure reduces to 3 keV from 11 keV of outer regions, implying that the Phoenix cluster has a cool core. Moreover, McDonald et al. (2015) reported bipolar X-ray cavities, which are often seen along with AGN activities in several nearby cool-core clusters including the Perseus cluster (Fabian et al. 2011). Therefore, AGN feedback seems to be taking place in the Phoenix cluster, without suppressing the massive star-formation and the rapid black-hole growth.

Taking a close look at this cluster will therefore give us unique understanding of the co-evolution of the ICM, the BCG, and the SMBH. Key information missing so far is whether or not there are radio jets/lobes, which are firm evidence of AGN feedback activities. Hogan et al. (2015a, 2015b) presented comprehensive studies of the radio properties and variabilities of BCGs. A relatively steep spectrum would be evidence of radio jets/lobes, while AGN core emission indicates a flatter spectrum, particularly at high frequencies. A more straightforward way to find jets/lobes is to resolve potential radio emissions spatially. van Weeren et al. (2014) reported that there is diffuse radio emission in the Phoenix cluster; however, radio jets/lobes have never been resolved. There has only been one long-baseline radio observation; a 16 cm observation of the Australia Telescope Compact Array (ATCA) with the longest 6 km array configuration (Project C2585). The authors reduced the data, however no structure was resolved even with the finest beam size of  $6''.92 \times 3''.84$  at the highest band of 3.1 GHz of the observation.

In this paper, we report the first sub-arcsecond resolution centimeter observation of the Phoenix cluster center. We chose the 15 mm band, which has never been used for this cluster and is the best suited to our objective because it is possible to thereby perform high-resolution observation. We resolved emissions from the AGN core and radio lobes successfully. This paper is organized as follows. We summarize our observation and data reduction in section 2. Results are shown in section 3, where we combine the data of Atacama Large Millimeter/submillimeter Array (ALMA) Band 3. Our discussion is presented in section 4, referring to the archival data of radio, optical, and X-ray observations so as to extend our discussion for the origin of the radio emissions we detected with ATCA. Our conclusion is

**Table 1.** Summary of observing specifications of ATCA.

Pointing (right ascension)	23 <sup>h</sup> 44 <sup>m</sup> 44 <sup>s</sup>
Pointing (declination)	−42°43′15″
Date and time 1 (UT)	2017 November 1 06:30–16:30
Date and time 2 (UT)	2017 November 2 06:30–16:30
Maximum baseline	6 km
Center frequency* (MHz)	17000, 19000
Bandwidth* (MHz)	2048, 2048
Setup calibrator	2251+158
Flux calibrator	1934–638
Bandpass calibrator	1921–293
Pointing/gain/phase calibrator	2333–415
Target on-source time (min)	760

\*CABB recorded two IF bands.

made in section 5. Unless otherwise specified, we consider the standard  $\Lambda$ CDM cosmology model with the cosmological parameters  $H_0 = 70 \text{ km s}^{-1} \text{ Mpc}^{-1}$ ,  $\Omega_M = 0.3$ , and  $\Omega_\Lambda = 0.7$ , leading to  $1'' \sim 6.7 \text{ kpc}$  at the source redshift of  $z = 0.596$ .

## 2 Observation and data reduction

Our observations were made with ATCA in 2017 November 1 and 2 (Project C3190, see table 1). The total observing times of the target were 360 minutes on November 1 and 400 minutes on November 2. The 6A array configuration was adopted, where all six antennas were mounted in the east–west track with the 6 km baseline at the maximum. The 1 M-0.5 k Compact Array Broadband Backend (CABB, Wilson et al. 2011) receiver mode was selected to utilize the 2048 channels with a 1 MHz spectral window at the 15 mm band, and full spectro-polarimetric data were recorded. Two intermediate frequencies (IFs) were set at the center frequencies of 17000 MHz for IF1 and 19000 MHz for IF2. The field of view was 2'.8 (2'.5) for IF1 (IF2), and the largest well-imaged structure was  $\sim 32''$  at 18 GHz (see sub-subsection 1.7.1 of the ATCA Users Guide).<sup>1</sup>

On each day, we observed the initial setup calibrator 2251+158 for 30 minutes, the flux-scale calibrator 1934–638 for six minutes, the bandpass calibrator 1921–293 for six minutes, a repetitive sequence, and the gain/phase calibrator 2333–415 for two minutes in this order. The repetitive sequence included observations of the pointing calibrator 2333–415 for two minutes, the gain/phase calibrator 2333–415 for two minutes, and the target for eight minutes, where 2333–415 is sufficiently bright (699 mJy at 15 mm) and close ( $2''.01$  from the target). The sequence was repeated nine times on November 1 and 10 times on November 2. This long-time tracking provided

us with good UV coverage. The system temperature was around 45 K (meridian passage)–82 K (setting) and those were stable during the observing days.

Data reduction was performed with the MIRIAD software (Sault et al. 1995) version 1.5 following the standard procedures, unless otherwise specified. All data were loaded using the MIRIAD task ATL0D with options BIRDIE, XYCORR, RFIFLAG, OPCORR, and NOAUTO. Edge 40 channels (32 MHz bandwidth) were removed by UVFLAG. We performed PGFLAG iteratively until any radio frequency interferences (RFIs) disappeared from the visibility plots. We adopted a modern flagging recipe in which we looked at visibility variations of Stokes V at first (sub-subsection 4.3.5 of the ATCA Users Guide). The band-pass solution was made by MFCAL using 1921–293. The solution was transferred to 2333–415 using GPCOPY, and then GPCAL was carried out to obtain the gain and phase solutions, with options XYVARY and QUSOLVE. The solution was transferred to 1934–638, and GPCAL was carried out to obtain the absolute flux scale, with options XYVARY, QUSOLVE, and NOPOL. The error of the absolute value was computed by bootstrap estimation using GPBOOT, from 1934–638 to 2333–415. Finally, all solutions were applied to the target data from 2333–415 using GPCOPY.

The visibility was transformed into real-space images using INVERT, where the robustness parameter,  $r$ , was examined from 0.5 to 2.0 to check the trade-off between the angular resolution and the image rms noise. The beam full-width at half-maximum (FWHM) of major/minor axes and the beam position angle are  $1'.03 \times 0'.46$  and  $6^\circ.5$ , respectively, at 18 GHz with  $r = 0.5$ . The images were cleaned by the multi-frequency CLEAN task MFCLEAN, where we chose the best iteration number which minimized the rms noise in the cleaned image. Using the brightest compact source at the center of the image (Source C1, see the next section), we performed phase self-calibration three times with the solution intervals of 15 minutes, five minutes, and one minute, updating the CLEAN model. The self-calibration improved the signal-to-noise ratio ( $S/N$ ) of Source C1 from 251 to 365. We finally achieved an image rms noise level almost comparable to the theoretical value, and found no significant emission of Stokes Q or U in the image. The upper limits (the  $1\sigma$  noise levels) are  $0.00639 \text{ mJy beam}^{-1}$  and  $0.00640 \text{ mJy beam}^{-1}$  for Stokes Q and U, respectively, with  $r = 2.0$ .

## 3 Results

### 3.1 Synthesized images

The top panel of figure 1 shows an image at 18 GHz, which corresponds to the rest-frame frequency of 28.7 GHz at

<sup>1</sup> ([https://www.narrabri.atnf.csiro.au/observing/users\\_guide/html/atug.html](https://www.narrabri.atnf.csiro.au/observing/users_guide/html/atug.html)).

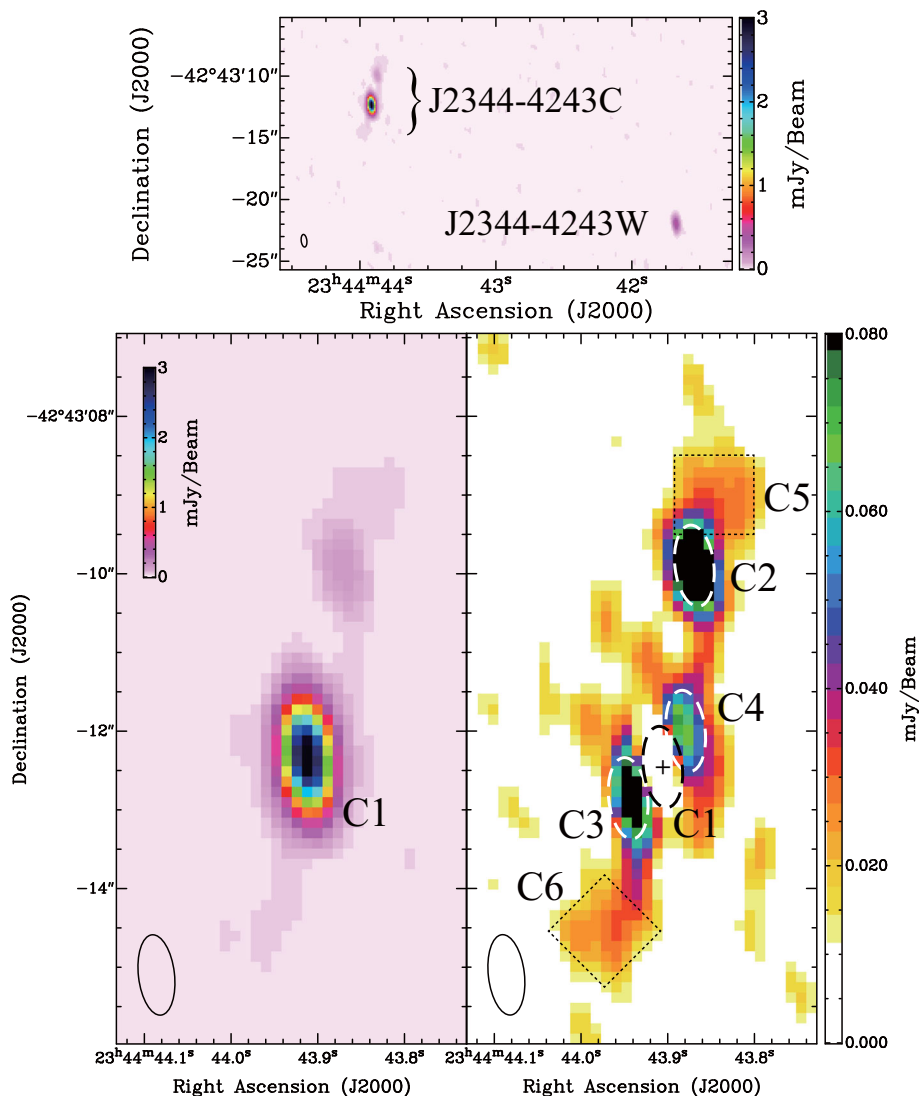


**Fig. 1.** (Top) ATCA 18 GHz total intensities (Stokes I) map of the Phoenix cluster of galaxies. (Bottom left) An enlarged map around J2344–4243C. (Bottom right) Same as bottom left but Source C1 (the black dashed ellipse) is subtracted. Also shown are Sources C2, C3, and C4, as white dashed ellipses. The dotted boxes with  $1'' \times 1''$  indicate the northern (C5) and southern (C6) diffuse emissions (see the text). The image rms noise level ( $1\sigma$ ) is  $0.00612 \text{ mJy beam}^{-1}$ . The bottom-left ellipse of each panel indicates the synthesized beam size. (Color online)

$z = 0.596$ , with a 4096 MHz bandwidth and  $r = 0.5$ . We find two radio components. The brightest, extended component, J2344–4243C, is located at the center of the Phoenix cluster and is associated with the BCG. The other, compact component, J2344–4243W or Source W, is  $26''.25$  away from the cluster center to the west. A zoom-in map of J2344–4243C is shown in the bottom left-hand panel of figure 1. There is a compact source, J2344–4243C1 or Source C1 hereafter, at the center.

We evaluated flux densities of Sources C1 and W using the MIRIAD task `IMFIT` with the option `OBJECT=POINT`. We obtained flux densities of  $3.395 \pm 0.132 \text{ mJy}$  for Source C1 and  $0.478 \pm 0.019 \text{ mJy}$  for Source W, both at 18 GHz. We subtracted Sources C1 and W from the image, and the resultant residual map is shown in the bottom right-hand

panel of figure 1. We clearly see some striking features in the residual map. First, there is a bright spot in the north of Source C1. We label the spot as Source C2. Secondly, we see two spots near Source C1. We label them as Sources C3 and C4. Thirdly, including Sources C3 and C4, there are diffuse emissions around the center. Finally, we see another two diffuse emissions in the north (labelled C5) and south (C6). They connect to central diffuse emission with straight bar-shape structures.

As with Sources C1 and W, Sources C2, C3, and C4 seem to be unresolved sources. Using the same MIRIAD task as for Source C1, we evaluated the flux densities of  $0.147 \pm 0.026 \text{ mJy}$ ,  $0.108 \pm 0.010 \text{ mJy}$ , and  $0.077 \pm 0.015 \text{ mJy}$  for Sources C2, C3, and C4, respectively, at 18 GHz.

All of the features mentioned in this subsection are also seen in the image made with  $r = 2.0$ . Those features are simply blurred, because of the worse angular resolution by 40%. The image has the better image rms noise level ( $1\sigma$ ) of  $0.00482 \text{ mJy beam}^{-1}$  compared to  $0.00612 \text{ mJy beam}^{-1}$  with  $r = 0.5$ . We tried various self-calibration procedures with different solution intervals for phase and gain, and confirmed that the labelled structures and the central extended emission remain. Therefore, we conclude that those features are all real.

With the total intensity and the upper limit of the polarized intensity,  $P = \sqrt{Q^2 + U^2}$ , we got the upper limits of the polarization fraction,  $P/I$ . Those are 0.27%, 5.94%, 11.3%, 18.1%, and 1.89% of Sources C1, C2, C3, C4, and W, respectively, at 18 GHz.

### 3.2 Frequency spectra

The frequency spectrum is a clue to understanding the radiation mechanism, which will be discussed in subsection 4.1. In order to quantify the spectrum, we define the spectral index,  $\alpha$ , of the flux-density spectrum as  $I_\nu \propto \nu^\alpha$ , where  $\nu$  is the frequency. In order to estimate the in-band spectral index, we made four images whose center frequencies were 16488 MHz, 17512 MHz, 18488 MHz, and 19512 MHz, each with a 1024 MHz bandwidth. With a simple power-law form, we carried out the error-weighted least-squares fit of the four data points, which are shown in figure 2. We obtained an in-band spectral index of  $\alpha = -0.50$  for the brightest Source C1. The other Sources showed in-band flux fluctuations due likely to calibration errors and are too faint to derive the in-band spectral index.

In order to obtain wideband spectra of the resolved sources, we combined ALMA Band 3 data of the Phoenix cluster (see Kitayama et al. 2020 for details). The center frequency is 92 GHz and the beam FWHM is  $1''.9 \times 1''.6$  (using  $>30k\lambda$  baselines). In the ALMA continuum map, four radio sources are detected with coordinates shown in table 2. We confirm that the coordinates of the brightest and second-brightest ALMA sources are identical to the coordinates of Sources C1 and W, respectively, where the statistical positional uncertainty of Source C1 is  $\sim(\text{beam size})/\sqrt{S/N} \sim 1''/\sqrt{365} \sim 0''.05$  for ATCA ( $0''.004$  for ALMA), and that of Source W is  $0''.11$  for ATCA ( $0''.05$  for ALMA). Therefore, we conclude that they are cross-matched and the coordinate systems of the two observations are identical at a  $0''.05$  level. Based on this fact, the declination offset of Source C2 between ATCA and ALMA is less than the  $3\sigma$  level; the position uncertainty of Source C2 is  $0''.2$  for ATCA ( $0''.1$  for ALMA). We also confirm that the position of Source C3 matches between ATCA and ALMA within a similar uncertainty.

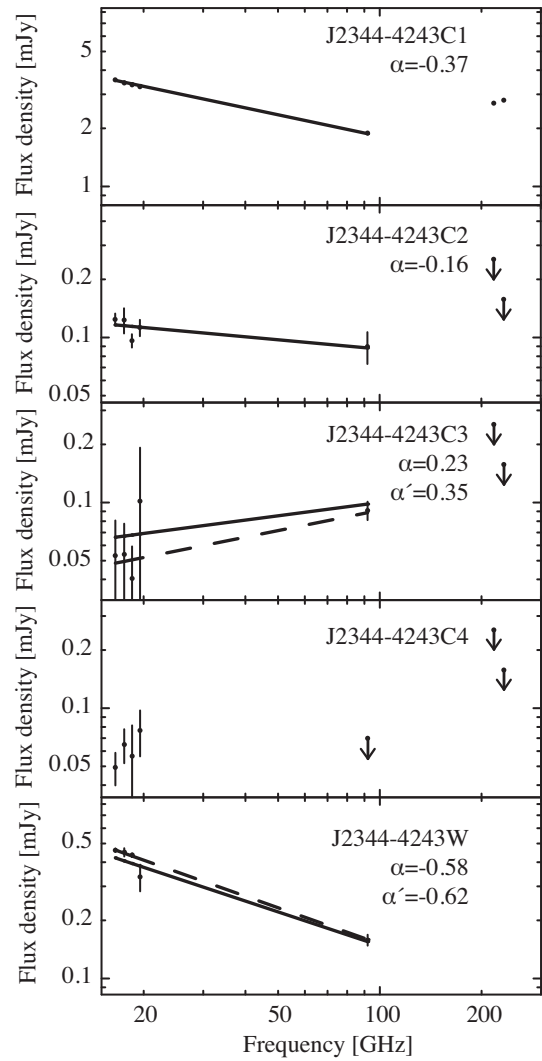


**Fig. 2.** Frequency spectra of resolved sources. ATCA 18 GHz, ALMA 92 GHz, 217.7 GHz, and 232.6 GHz data are shown. Arrows are the upper limits of ALMA 217.7 GHz and 232.6 GHz. The solid lines show the best power-law fits and those spectral indices,  $\alpha$ , are indicated. Also shown as the dashed lines and  $\alpha'$  are the best fits and the spectral indices, respectively, except the data at 19.5 GHz.

**Table 2.** Coordinates of radio sources.

Source ID	Right ascension		Offset (")
	ATCA (J2000.0)	ALMA (J2000.0)	
C1	23 <sup>h</sup> 44 <sup>m</sup> 43 <sup>s</sup> .900	23 <sup>h</sup> 44 <sup>m</sup> 43 <sup>s</sup> .905	-0.005
C2	23 <sup>h</sup> 44 <sup>m</sup> 43 <sup>s</sup> .857	23 <sup>h</sup> 44 <sup>m</sup> 43 <sup>s</sup> .887	-0.030
C3	23 <sup>h</sup> 44 <sup>m</sup> 43 <sup>s</sup> .926	23 <sup>h</sup> 44 <sup>m</sup> 43 <sup>s</sup> .973	-0.047
C4	23 <sup>h</sup> 44 <sup>m</sup> 43 <sup>s</sup> .869	No detection	
W	23 <sup>h</sup> 44 <sup>m</sup> 41 <sup>s</sup> .666	23 <sup>h</sup> 44 <sup>m</sup> 41 <sup>s</sup> .661	0.005
Source ID	Declination		Offset (")
	ATCA (J2000.0)	ALMA (J2000.0)	
C1	-42° 43' 12".508	-42° 43' 12".548	-0.040
C2	-42° 43' 10".106	-42° 43' 10".684	-0.578
C3	-42° 43' 12".965	-42° 43' 13".493	-0.528
C4	-42° 43' 12".131	no detection	
W	-42° 43' 22".090	-42° 43' 22".139	-0.049

The results of the spectral index measurement using ATCA 18 GHz and ALMA 92 GHz data are shown in figure 2. We obtain a flatter ( $\alpha = -0.37$ ) spectrum for Source C1 compared to the in-band spectrum (with  $\alpha = -0.50$ ). Source C2 has a flat spectrum with  $\alpha = -0.16$ . We also plot ALMA Band 6 (Russell et al. 2017) upper limits to confirm the consistency of the flat spectrum, though we do not obtain strong constraints from them. For Source C3, we obtain a positive slope,  $\alpha = 0.23$  and  $0.35$ , with and without the data at 19.5 GHz in the fit, respectively, where there is a large flux error at 19.5 GHz. The positive slope is consistent with the upper limits of ALMA Band 6. At a  $5\sigma$  upper limit (or  $0.07$  mJy) at 92 GHz, the spectrum of Source C4 could be flat. Otherwise, it has a negative slope. Finally, for Source W,  $\alpha = -0.58$  and  $-0.62$  with and without the data at 19.5 GHz in the fit, respectively.

## 4 Discussion

### 4.1 Possible radiation mechanisms

Synchrotron radiation from cosmic-ray (CR) electrons is predominant at centimeter wavelengths in general (e.g., Akahori et al. 2018a). Such cosmic rays can be made by AGN and shock waves associated with jets. Typical spectral indices of a radio lobe and an AGN core (or a quasar) are  $\alpha \sim -0.7$  and  $\alpha \sim 0$ , respectively (see, e.g., Farnes et al. 2014). The latter flat spectrum is thought to be produced by the synchrotron self-absorption of the dense circumnuclear medium known as a Gigahertz Peaked Source (GPS), which is often seen in BCGs (Hogan et al. 2015a, 2015b). In addition, recent VLBI observations of the 3C 84 jet suggest strong synchrotron absorption and a flip of the motion (Nagai et al. 2017; Hiura et al. 2018; Kino et al. 2018). It was interpreted that these features are caused by molecular clumps with the typical number density of  $10^3$ – $10^5$  cm $^{-3}$ . Therefore, a flat synchrotron spectrum may also be produced by dense molecular clumps. Note that in a case of a GPS-like component the spectrum has a peak at a frequency lower than that of our observations, and the spectrum has a positive gradient in an even lower frequency because of the frequency-dependence of the absorption.

Free-free emission from thermal electrons can contribute to the radiation at centimeter wavelengths. Free-free emission has a flat spectrum and can be more significant than synchrotron radiation at higher frequencies (see, e.g., Condon 1992 for a review). Thermal electrons emitting free-free emission exist in warm ionized medium of the interstellar medium (ISM) ionized by radiation from massive stars and AGN, and supernova shocks. In fact, McDonald et al. (2014) suggested that the low-ionization lines from a complex emission-line nebula at the BCG are

consistent with photo-ionization by young stars. Another origin of a warm ionized medium may be a transient warm-ionized ICM of the cooling flow at the cluster center.

The spinning dust emission (Draine & Lazarian 1998a, 1998b) can also contribute to the radiation at centimeter wavelengths, if a massive amount of small dust grains exists. The emission can have a flat or positive spectral index around the relevant frequency in general. The brightness of the spinning dust emission is estimated to be  $O(0.01)(n_{\text{H}}/10^2 \text{ cm}^{-3})$  mJy beam $^{-1}$  around 15–30 GHz, where  $n_{\text{H}}$  is the hydrogen number density. Even higher-frequency, galactic thermal dust emission becomes predominant, showing a steep, positive slope. The spinning dust emission should spatially correlate with the thermal dust emission.

In the following subsections, we discuss the origins of the observed radio sources near the cluster center. We focus on the compact emissions at the BCG, the extended emission around the BCG, and the diffuse emission extending to the north and south, in that order.

### 4.2 AGN core and jets (Sources C1, C3, and C4)

Source C1 is a compact source and is located at (RA, Dec) = (23<sup>h</sup>44<sup>m</sup>43<sup>s</sup>:90,  $-42^{\circ} 43' 12''.51$ ) (J2000.0) with a positional accuracy of  $\sim 0''.05$ . We confirmed that the coordinate is identical to the X-ray brightness center reported by McDonald et al. (2015) (RA, Dec) = (23<sup>h</sup>44<sup>m</sup>43<sup>s</sup>:94,  $-42^{\circ} 43' 12''.52$ ) (J2000.0), so that Source C1 is likely the AGN core. McDonald et al. (2014) reported the coordinate of the optical brightness center of the BCG as (RA, Dec) = (23<sup>h</sup>44<sup>m</sup>43<sup>s</sup>:96,  $-42^{\circ} 43' 12''.20$ ) (J2000.0). The position of the BCG center can be identical to that of Source C1, according to the fact that there is an astrometry offset between the Hubble Space Telescope (HST) and ATCA/ALMA, ( $\delta\text{RA}, \delta\text{Dec}$ ) = ( $-0''.08, +0''.3$ ) (Dunlop et al. 2017), which is very close to the offset we found.

Sources C3 and C4 are located near the AGN core and they are along the north–south diffuse emission with straight bar-shape structures. These structures suggest the idea that Sources C3 and C4 are bipolar jets from the AGN, where their flat or positive spectra could be explained by self-absorbed synchrotron radiation. It is interesting that the spectral index of Source C3 is different from that of Source C4, although they are located at the point-symmetric positions with respect to Source C1. Thus, there should exist inhomogeneous structure around the AGN.

Figure 3 shows the broadband radio spectrum of J2344–4243C. We plot the archival data of Murchison Widefield Array (MWA) The GaLactic and Extragalactic All-sky MWA survey (GLEAM) (Hurley-Walker et al. 2017) at 76–227 MHz, where J2344–4243C is not

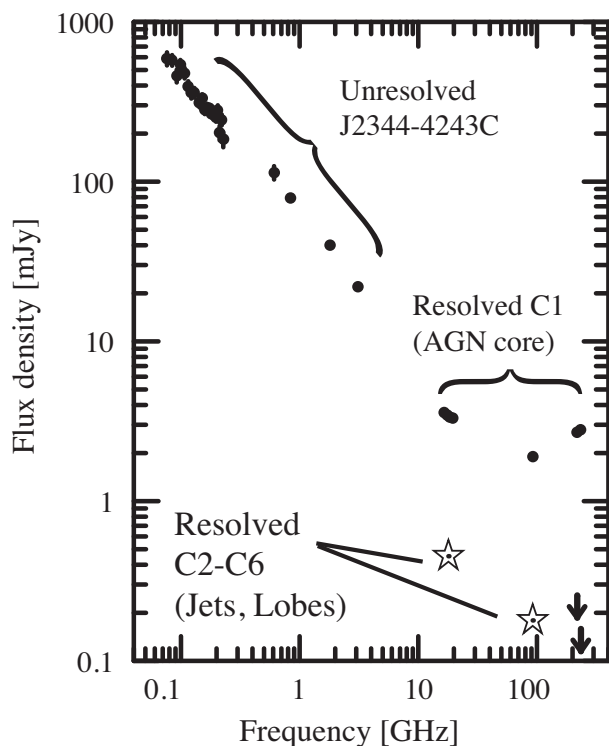


**Fig. 3.** Broadband radio spectrum of J2344–4243C. The integrated flux densities are taken from MWA GLEAM (76–227 MHz) (Hurley-Walker et al. 2017), GMRT (610 MHz) (van Weeren et al. 2014), SUMSS (843 MHz) (Bock et al. 1999), and ATCA (1.8 GHz and 3.1 GHz). These observations did not resolve the substructures (C2–C6). Also shown are the data of ATCA (18 GHz, this work), ALMA Band 3 (92 GHz) (Kitayama et al. 2020), and ALMA Band 6 (218 GHz and 233 GHz) (Russell et al. 2017). For those three data, the flux densities of Source C1 are shown as black dots. Open stars show the sum of the flux densities for C2, C3, C4, C5, and C6 at 18 GHz and the sum of C2 and C3 at 92 GHz. Arrows indicate the upper limits at 218 GHz and 233 GHz.

spatially resolved. The data indicate the spectral index of  $\alpha(\text{GLEAM}) = -0.929$ . Such a slope is also found by van Weeren et al. (2014) who reported the spatially-integrated flux density of  $114.0 \pm 11.0$  mJy at Giant Metrewave Radio Telescope (GMRT) 610 MHz and obtained  $\alpha(\text{GMRT}) = -0.84$  for GMRT 156 MHz and 610 MHz. However, McDonald et al. (2014) reported the steeper spectrum with the spectral index of  $\alpha = -1.35$ , based on the unresolved data of Sydney University Molonglo Sky Survey (SUMSS) (Bock et al. 1999) 843 MHz ( $79.2 \pm 3.0$  mJy) and ATCA 16 cm. A similar steep spectrum of  $\alpha = -1.2$  is obtained from the previous ATCA observation (ID: C2585) with the total intensities 40 mJy at 1.8 GHz and 22 mJy at 3.1 GHz.

While the above steep spectrum has been observed below several GHz, we found a shallower spectrum with the spectral indices of  $\alpha(\text{ATCA}) = -0.50$  and  $\alpha(\text{ATCA} + \text{ALMA}) = -0.37$  in the frequency range of  $\sim 10$ –100 GHz. The broadband spectrum is thus difficult to explain with a

single power law. We suspect that the broadband spectrum of Source C1 consists of at least two components. One, which dominates emission at  $\sim 10$ –100 GHz, can be self-absorbed synchrotron radiation like a GPS source. In fact, the AGN core is highly obscured (Ueda et al. 2013), suggesting significant absorbers around the AGN. The other can be optically-thin synchrotron radiation dominating emission below several GHz. We show the sum of the flux densities for the other resolved components in figure 3. The sum is about an order-of-magnitude fainter than that of Source C1, providing an upper limit of the strength of spectrum cut-off, i.e., the population of the highest-energy electrons emitting synchrotron radiation.

We also plot the data of ALMA 233 GHz and indicates that the flux density of Source C1 increases as the frequency increases. McDonald et al. (2014) displayed three spectral energy distribution (SED) models for the BCG; elliptical galaxy, Type 2 QSO, and M 82-like star-burst galaxy. ALMA 233 GHz is consistent with the Type 2 QSO model (not shown, see McDonald et al. 2014), which is also consistent at optical bands. Another possibility is that the GPS component is time-variable (Hogan et al. 2015b). In this case, the lower flux in Band 3 (observed in 2016) compared to ATCA 18 GHz and Band 6 (observed in 2014) is due to time variation, and these emissions are explained by a single GPS.

### 4.3 Extended emissions surrounding the AGN

In addition to Sources C1, C3, and C4, our ATCA observation suggests extended emissions which seem to surround the AGN core (see figure 1). In order to look for possible counterparts, we made superposed images with ALMA CO(3–2) and the ALMA 233 GHz continuum (Russell et al. 2017), and HST F814W (814 nm, *I* band, McDonald et al. 2015; the coordinate offset is not corrected) in figure 4. Here, the CO(3–2) emission indicates star-forming molecular gas. The 233 GHz continuum represents mostly the dust distribution. The 814 nm emission is a tracer of stars and star formation. Star formation implies a UV radiation field of OB stars and their supernovae, i.e., the existence of the warm ionized gas and cosmic-ray electrons. The image clearly indicates that there is CO(3–2), 233 GHz continuum, and/or 814 nm emission around Source C1, suggesting the presence of a large amount of molecular gas, dust grains, and non-thermal electrons, all of which can contribute radio emission at 18 GHz (28.7 GHz at  $z = 0.596$ ). Therefore, the extended emission surrounding the AGN could be the superposition of jets, ISM, and circumgalactic medium.

In the northwestern part of the central extended emission including Source C4, the 233 GHz emission (dust) is

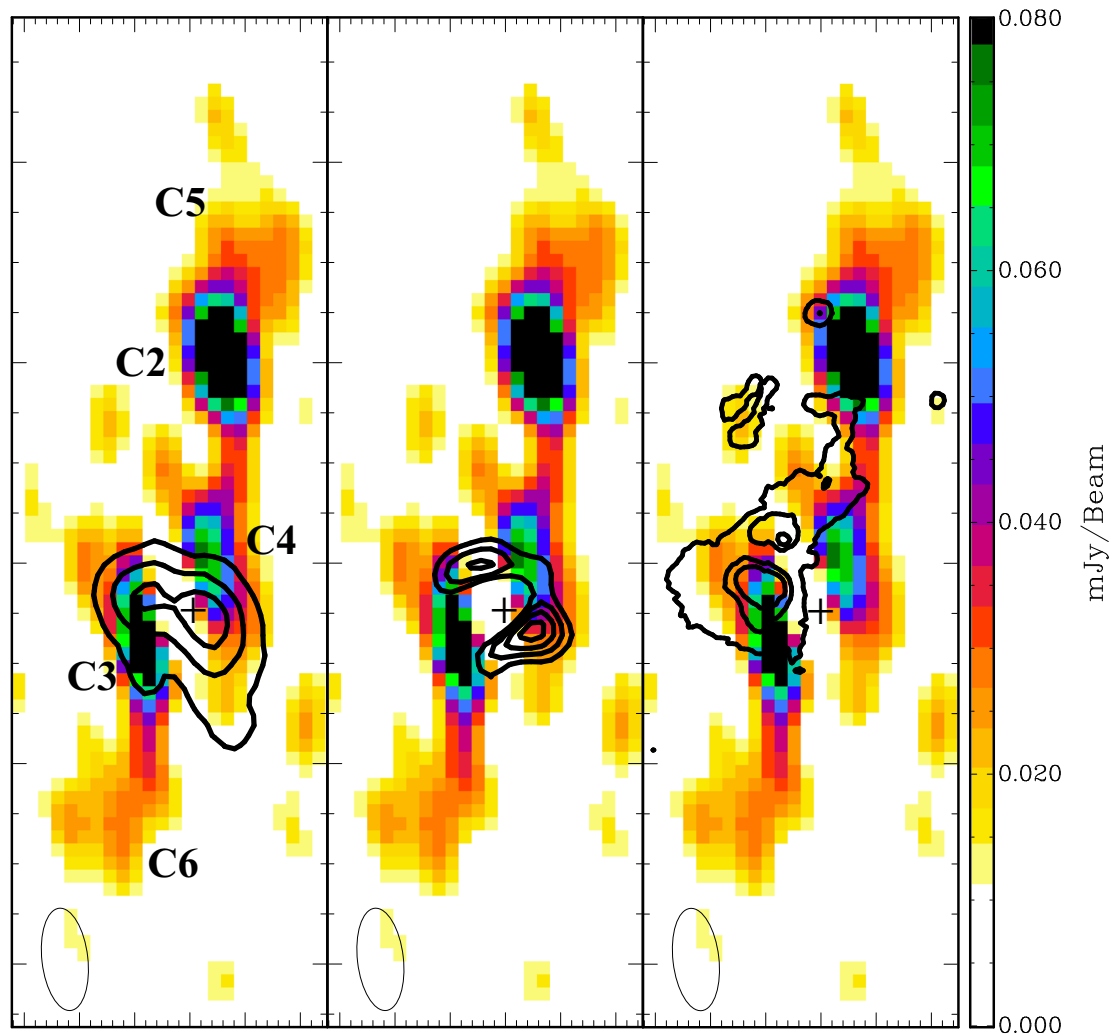


**Fig. 4.** Superposed images of the Phoenix cluster center. The cross indicates the position of Source C1, which is subtracted from the background image. The synthesized beam pattern is shown at the bottom right. (Left) The ALMA CO(3–2) integrated intensity map (Russell et al. 2017). The contour levels are 0.7, 1.5, and 3.1 mJy beam<sup>-1</sup>. (Middle) The ALMA Band 6 (233 GHz) continuum contour map (Russell et al. 2017), where the primary compact source at the peak of the continuum intensity is subtracted. The contour levels are 0.5, 1.0, 1.5, and 2.0 mJy beam<sup>-1</sup>. (Right) The HST 814 nm contour map. The contour levels are 0.2, 0.7, and 1.5 in arbitrary units. (Color online)

bright. Therefore, radio emission (18 GHz and 92 GHz) of Source C4 could be the superposition of jet synchrotron and dust emission. It should be noted that the 814 nm emission (stars) is not bright and the difference between dust emission and 814 nm emission cannot be explained by relative coordinate errors (by 0'.3) between the radio and optical observations. One possible explanation of this difference is that there is an inclined BCG and its gas disk obscures star lights from the southwestern region, i.e., a dust lane. This potential galactic disk is partly seen as the high-density molecular gas of CO(3–2). In fact, Russell et al. (2017) claimed an east–west velocity gradient which is consistent with ordered motion or rotation about the AGN, although we need a higher spatial resolution CO observation in order to confirm the existence of such a putative disk. If it is a case

of a dust lane, the radio jet is edge-on and rather parallel to the disk.

In the southeastern part of the central extended emission including Source C3, the 814 nm emission (stars) is bright but the 233 GHz continuum emission (dust) is not. Therefore, the radio emission (18 GHz and 92 GHz) of Source C3 could be the superposition of jet synchrotron and free-free emission from the warm gas ionized by UV radiation from massive stars. Meanwhile, the spinning dust emission could be minor, because a feature-less, flatter extinction curve implies that the size distribution of the dust is skewed toward larger grains (McDonald et al. 2015), i.e., the spinning dust emission from small dust grains may be less important compared to the typical case (Draine & Lazarian 1998a, 1998b).



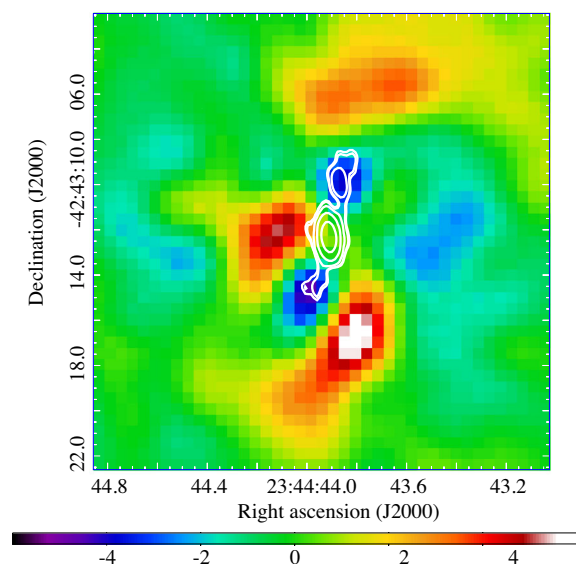


**Fig. 5.** Superposed image of the Phoenix cluster. The background color shows the Chandra X-ray surface brightness residual in arbitrary units. The white contours are ATCA 18 GHz emission of 0.02, 0.025, 0.05, 0.2, and 1 mJy beam<sup>-1</sup>. (Color online)

#### 4.4 Radio lobes (sources C2, C5, and C6)

We examine ICM distribution around the AGN and compare it with the 18 GHz radio distribution. For this purpose, we made an X-ray surface brightness residual map using Chandra X-ray Observatory archival data of the Phoenix cluster (ObsID: 13401, 16135, and 16545). The energy range of soft X-rays, 0.5–2.0 keV, is adopted to reduce the contamination emission from the Type 2 QSO. With the same dataset and energy range, McDonald et al. (2015) already showed the residual map, but we reprocessed the data using Chandra Interactive Analysis of Observations (CIAO; Fruscione et al. 2006) version 4.9 and new calibration database (CALDB) version 4.7.8. McDonald et al. (2015) modeled the X-ray surface brightness with a two-beta model. We modeled the X-ray surface profile in  $1'' < r < 5''$  from the position of the AGN in X-rays using an ellipse model (Ueda et al. 2017, 2018), where the position angle is  $-86^\circ$  and the axis ratio of the obtained ellipse is 0.92. We calculated the mean profile of the X-ray surface brightness using the parameter of the obtained ellipse and subtracted it from the original X-ray surface brightness map.

The resultant X-ray residual map superposed with the 18 GHz radio image is shown in figure 5. The residual structure is in broad agreement with that shown by McDonald et al. (2015). Interestingly, both the northern and southern structures are aligned with X-ray negative regions (i.e., cavities). This supports that Sources C5 and C6 are radio lobes, as often seen in the nearby Universe. The northern extended structure of HST 814 nm broadly aligns with the northern bar structure of the 18 GHz emission, suggesting

that a part of the star-forming gas is blown away from the BCG by the jet.

We estimate non-thermal energy (cosmic-rays and magnetic field) associated with the diffuse radio emission under the assumption of energy equipartition (see Akahori et al. 2018b). Our detection of 0.03 mJy beam<sup>-1</sup> at 18 GHz for Sources C5 and C6 and representative values ( $p, \gamma_{\min}, \gamma_{\max}, D_{\text{los}} = (3, 200, 3000, 10 \text{ kpc})$ ) gives  $B \sim 23.4f^{1/4} \mu\text{G}$  or the cosmic-ray electron density  $n_{\text{ce}} \sim 7.10 \times 10^{-8}f^{-1/2} \text{ cm}^{-3}$ . Here,  $p$  is the index of cosmic-ray electron energy distribution ( $p = 3$  corresponds to  $\alpha = -1$  in this paper),  $\gamma_{\min}$  and  $\gamma_{\max}$  are the minimum and maximum Lorentz factor of the cosmic-ray electrons, respectively, and  $D_{\text{los}}$  is the depth of the emission along the line of sight.  $f - 1$  is the energy fraction of CR-ions with respect to CR-electrons (see, e.g., Pfrommer & Enßlin 2004; Akahori et al. 2018b). Although the value of  $f$  is unclear, it is  $O(100)$  for radio halos in Perseus and Coma clusters (Pfrommer & Enßlin 2004). The resultant magnetic-field strength and the cosmic-ray electron density are much larger than those known in nearby cluster environments, supporting that these diffuse emission is radio lobes.

We have checked that there is no clear optical counterpart of Source C2. Since it is a compact source, one may consider that Source C2 is an unresolved radio galaxy or a quasar. However, supposing the population of 0.1 mJy sources at 18 GHz (e.g., Wilman et al. 2008), the probability that an extragalactic radio source overlaps a 1-arcsec<sup>2</sup> patch is  $1.2 \times 10^{-3}\%$ , which is very low. Therefore, a reasonable interpretation is that Source C2 is an object associated with the diffuse emission and is likely a bright knot and/or kinks of jets seen in, for example, the BCGs of Abell 1795 and Abell 2597. In other words, Sources C2, C5, and C6 are an older Fanaroff and Riley Class II (FR II) and Sources C3 and C4 are a younger FRI of another two-side jet. Jet precession may explain the fact that the axes of C2-C1 and C4-C1-C3 are not exactly aligned with each other.

The diffuse sources C5 and C6 are located  $\sim 13 \text{ kpc}$  and  $\sim 20 \text{ kpc}$  away from Source C1, respectively. Assuming that the shock waves caused by jets are propagating with a sound velocity of  $900 \text{ km s}^{-1}$  (3 keV, Ueda et al. 2013), we obtain 12 Myr and 18 Myr for the diffuse sources C5 and C6, respectively. Moreover, if C3 and C4 are newly-born jets, their ages are  $\sim 1 \text{ Myr}$ . Therefore, if Sources C5 and C6 are radio lobes of old jets and C3 and C4 are newly-born jets, the duty cycle of AGN jet is  $O(10) \text{ Myr}$ . It is interesting that the new jets may link with young ( $\sim \text{Myr}$ , McDonald et al. 2015) stellar populations; launches of the new jets and massive star formation happened at the nearly same time. Our observation did not find even older radio jets or lobes. If there were multiple jet launches in the past, with

future high-sensitivity and high angular-resolution X-ray observations we could see the ripples of X-ray cavities as seen in the Perseus cluster (Fabian et al. 2006).

We estimate the rest-frame, monochromatic radio power at the rest-frame frequency  $\nu'$  as

$$L_{\nu'} = 4\pi D_L^2 \Omega (1+z)^{-1} S_\nu \left[ \frac{\nu'}{(1+z)} \right]^\beta, \quad (1)$$

where  $D_L$  is the luminosity distance,  $\Omega$  is the emission area,  $z$  is the redshift,  $S_\nu$  is the observed surface brightness at the observed frequency  $\nu$ , and  $\beta$  is the spectral index for  $S_\nu \propto \nu^\beta$ . We adopt  $D_L \sim 3.53 \text{ Gpc} \sim 1.089 \times 10^{26} \text{ m}$ ,  $\Omega = 1 \text{ arcsec}^2$  for Source C5 or C6,  $z = 0.596$ , and  $S_\nu = 0.03 \text{ mJy beam}^{-1}$  at 18 GHz with beam size  $0.537 \text{ arcsec}^2$  with  $r = 0.5$ . Assuming the spectral indices of  $\beta = -0.5$  and  $-1.0$ , the monochromatic radio powers at  $\nu' = 1.4 \text{ GHz}$  are  $L_{1.4} = 2.4 \times 10^{23} \text{ WHz}^{-1}$  and  $1.1 \times 10^{24} \text{ WHz}^{-1}$ , respectively. This radio power is close to the 50% percentile of the cumulative luminosity function for BCGs (Hogan et al. 2015a, 2015b).

We then estimate the radio luminosity,

$$L = \int_{\nu'_1}^{\nu'_2} L_{\nu'} d\nu'. \quad (2)$$

Integrating emission from  $\nu'_1 = 10 \text{ MHz}$  to  $\nu'_2 = 10 \text{ GHz}$  for  $\beta = -0.5$  and  $-1.0$ , we obtain  $L \sim 8.6 \times 10^{39} \text{ erg s}^{-1}$  and  $2.1 \times 10^{40} \text{ erg s}^{-1}$ , respectively. The derived radio power of the diffuse emission is not enough at all to compete with the X-ray radiative cooling loss,  $L_{\text{cool}, 100\text{kpc}} = 9.6 \times 10^{45} \text{ erg s}^{-1}$  (McDonald et al. 2015). Even if we integrate the whole northern emission including Sources C2, C4, C5, and a bar-shape structure, the radio luminosity increases only by a factor of 4. The derived radio power is also small compared to the jet power according to X-ray cavities,  $L_{\text{cavity}} = 2\text{--}7 \times 10^{45} \text{ erg s}^{-1}$  (McDonald et al. 2015), implying that the jet energy is dominated by kinetic energy.

## 5 Concluding remarks

SPT-CL J2344–4243 (the Phoenix cluster) located at the redshift of 0.596 has an extreme star-burst BCG at the cluster center. The BCG possesses a heavy SMBH surrounding a huge amount of cold gas. These features suggested the realization of the classical picture of cooling flow in the previous works. Previous X-ray observations indicated cool gas in the cluster core. They also showed X-ray cavities, suggesting the existence of AGN feedback often seen in nearby cool-core clusters. However, radio jets/lobes of AGN have never previously been spatially resolved.

We conducted an ATCA 15 mm observation of the Phoenix cluster center, and resolved emissions at/around AGN and emissions extending toward the north–south direction. At the cluster center, we find a compact radio source associated with the AGN. We also find two compact sources near the AGN, and they are likely newly-born jets. Moreover, surrounding the AGN, we find extended emission which could primary be synchrotron radiation partially absorbed by dense molecular clumps and free–free emission from the massive warm ionized gas. Because of difference between the potential dust distribution and the extended emission, the spinning dust emission from dusty circumgalactic medium could be secondary.

We discovered diffuse bipolar radio structures extending from the AGN of the BCG in the north–south direction. The locations of the radio structures are consistent with X-ray cavities, implying that they are radio jets/lobes of the AGN. We find a bright jet knot and/or kink candidate at the north. The lobe sizes are only 10–20 kpc and the ages could be less than a few tens of Myr. Moreover, if compact radio emissions near the center is from newly-born jets, those ages are  $\sim 1 \text{ Myr}$ . We point out that launches of new jets and massive star formation with young ( $\sim \text{Myr}$ , McDonald et al. 2015) stellar populations happened at the nearly same time in the past. Therefore, there may exist the same trigger which caused both activities. The monochromatic radio power of a radio lobe is estimated to be  $O(10^{23}) \text{ WHz}^{-1}$  at 1.4 GHz. We stress that this radio power is not enough to recover the X-ray cooling loss of the ICM.

Our study indicates that a sub-arcsecond scale angular resolution is required to study the radio emission at the center of the Phoenix cluster. Since the radio lobes should be synchrotron-dominated, a lower frequency observation has advantages in the signal-to-noise ratio. Naively, an angular resolution at 18 GHz with a 6 km baseline (this work) is equivalent to that at 0.9 GHz with a 120 km baseline, which will indeed be available with the phase 1 of the Square Kilometre Array (SKA)<sup>2</sup>. Therefore, this cluster can be a good case for the use of SKA.

## Note added in proof

After this paper was submitted, McDonald et al. (2019) submitted a paper and presented a radio continuum image in the 8–12 GHz X-band using the Karl G. Jansky Very Large Array (VLA). McDonald et al. (2019) found multiple radio sources. While the synthesized beam of the JVLA data is quite elongated, the brightest radio source of McDonald et al. (2019) seems to be associated with C1 + C3 + C4,

<sup>2</sup> (<https://www.skatelescope.org>).

and the northern radio source of McDonald et al. (2019) is associated with C2+C5.

## Acknowledgments

We thank the referees for their useful comments and suggestions. The Australia Telescope Compact Array is funded by the Commonwealth of Australia for operation as a National Facility managed by CSIRO. The scientific results of this paper are based in part on data obtained from the Chandra Data Archive: ObsID 13401, 16135, and 16545. This work was supported in part by JSPS KAKENHI Grant Numbers, JP15H03639(TA), JP15H05892 (MO), JP15K17614(TA), JP17H01110(TA), JP17H06130 (KK, RK), JP18K03693 (MO), JP18K03704 (TK), and by the Ministry of Science and Technology of Taiwan (grant MOST 106-2628-M-001-003-MY3) and by Academia Sinica (grant AS-IA-107-M01).

## References

- Akahori, T., & Masai, K. 2005, *PASJ*, 57, 419  
 Akahori, T., & Masai, K. 2006, *PASJ*, 58, 521  
 Akahori, T., et al. 2018a, *PASJ*, 70, R2  
 Akahori, T., et al. 2018b, *PASJ*, 70, 53  
 Bock, D., Large, M. I., & Sadler, E. M. 1999, *AJ*, 117, 1578  
 Canning, R. E. A., et al. 2014, *MNRAS*, 444, 336  
 Condon, J. J. 1992, *ARA&A*, 30, 575  
 Conselice, C. J., Gallagher, J. S., & Wyse, R. F. G. 2001, *AJ*, 122, 2281  
 Draine, B. T., & Lazarian, A. 1998a, *ApJ*, 508, 157  
 Draine, B. T., & Lazarian, A. 1998b, *ApJ*, 494, L19  
 Dunlop, J. S., et al. 2017, *MNRAS*, 466, 861  
 Fabian, A. C. 1994, *ARA&A*, 32, 277  
 Fabian, A. C. 2012, *ARA&A*, 50, 455  
 Fabian, A. C., et al. 2011, *MNRAS*, 418, 2154  
 Fabian, A. C., Sanders, J. S., Taylor, G. B., Allen, S. W., Crawford, C. S., Johnstone, R. M., & Iwasawa, K. 2006, *MNRAS*, 366, 417  
 Farnes, J. S., Gaensler, B. M., & Carretti, E. 2014, *ApJS*, 212, 15  
 Fruscione, A., et al. 2006, *SPIE Proc.*, 6270, 62701V  
 Hiura, K., et al. 2018, *PASJ*, 70, 83  
 Hogan, M. T., et al. 2015a, *MNRAS*, 453, 1201  
 Hogan, M. T., et al. 2015b, *MNRAS*, 453, 1223  
 Holtzman, J. A., et al. 1992, *AJ*, 103, 691  
 Hurley-Walker, N., et al. 2017, *MNRAS*, 464, 1146  
 Kino, M., et al. 2018, *ApJ*, 864, 118  
 Kitayama, T., et al. 2020, *PASJ*, 72, 33  
 Lewis, A. D., Stocke, J. T., & Buote, D. A. 2002, *ApJ*, 573, L13  
 Makishima, K., et al. 2001, *PASJ*, 53, 401  
 Masai, K., & Kitayama, T. 2004, *A&A*, 421, 815  
 McDonald, M., et al. 2012, *Nature*, 488, 349  
 McDonald, M., et al. 2014, *ApJ*, 784, 18  
 McDonald, M., et al. 2015, *ApJ*, 811, 111  
 McDonald, M., et al. 2019, *ApJ*, 885, 63  
 McDonald, M., Benson, B., Veilleux, S., Bautz, M. W., & Reichardt, C. L. 2013, *ApJ*, 765, L37  
 Nagai, H., Fujita, Y., Nakamura, M., Orienti, M., Kino, M., Asada, K., & Giovannini, G. 2017, *ApJ*, 849, 52  
 Ota, N., & Mitsuda, K. 2002, *ApJ*, 567, L23  
 Ota, N., & Mitsuda, K. 2004, *A&A*, 428, 757  
 Peterson, J. R., Kahn, S. M., Paerels, F. B. S., Kaastra, J. S., Tamura, T., Bleeker, J. A. M., Ferrigno, C., & Jernigan, J. G. 2003, *ApJ*, 590, 207  
 Pfrommer, C., & Enßlin, T. A. 2004, *MNRAS*, 352, 76  
 Russell, H. R., et al. 2017, *ApJ*, 836, 130  
 Ruszkowski, M., Brügggen, M., & Begelman, M. C. 2004, *ApJ*, 611, 158  
 Sanderson, A. J. R., O’Sullivan, E., & Ponman, T. J. 2009, *MNRAS*, 395, 764  
 Sault, R. J., Teuben, P. J., & Wright, M. C. H. 1995, in *ASP Conf. Ser.*, 77, *Astronomical Data Analysis Software and Systems IV*, ed. R. Shaw et al. (San Francisco: ASP), 433  
 Tamura, T., et al. 2001, *A&A*, 365, L87  
 Ueda, S., et al. 2018, *ApJ*, 866, 48  
 Ueda, S., Hayashida, K., Anabuki, N., Nakajima, H., Koyama, K., & Tsunemi, H. 2013, *ApJ*, 778, 33  
 Ueda, S., Kitayama, T., & Dotani, T. 2017, *ApJ*, 837, 34  
 van Weeren, R., et al. 2014, *ApJ*, 786, L17  
 Wilman, R. J., et al. 2008, *MNRAS*, 388, 1335  
 Wilson, E., et al. 2011, *MNRAS*, 416, 832